Optimization of Guided Weapon Designs with a Stochastic Objective Function Using a Genetic Algorithm

Ross B. Alexander[1], Andrew L. Kaminsky[2]

CFD Research Corporation, Huntsville, AL 35807, USA

In this paper, we demonstrate effective optimization on a stochastic objective function using a genetic algorithm and identification of several optimal guided weapon designs. The guided weapon model used in the objective function simulates a three-degree-of-freedom missile engaging with a two-degree-of-freedom constant-velocity target. We introduce both aleatoric and epistemic uncertainty in the model by imposing statistical distributions and upper and lower bounds on several inertial, atmospheric, and target parameters. We generate two small training target sets using a random sampling according to the specified distributions and bounds – one training set with 20 targets and another training set with 100 targets that is a proper superset of the set of 20 targets. An initial population of individual designs is randomly generated. Uncertain simulation parameters are randomly generated using the specified distributions and bounds and are paired to each target. The objective function is evaluated for every individual for each of the target-simulation parameter set pairs. The individual's fitness function is then computed as the mean miss distance over the target set and the design population is then evolved using the genetic algorithm. New uncertain simulation parameters are re-generated and are paired to each target in the same target set. The new design population's objective functions are evaluated for the updated target-simulation parameter set pairs, the fitness functions are evaluated, the design population is evolved, and the process is repeated for several generations until an optimal design is identified. We then generate two large testing target sets using the same random sampling according to the specified distributions and bounds – one testing set with 1,000 targets and another testing set with 10,000 targets that is a proper superset of the set of 1,000 targets. Like the training, a set of uncertain simulation parameters are randomly generated using provided distributions and bounds and paired to each target. Using this set of target-simulation parameter set pairs, we evaluate the performance of the optimal candidate. The miss distance empirical distribution functions are generated and Dvoretzky-Kiefer-Wolfowitz confidence bounds are employed to capture uncertainty in the underlying cumulative distribution functions. Additionally, areas-of-possible-intercept and areas-of-intercept are calculated. We demonstrate significant improvement over the baseline MATLAB model in three distinct cases of varying design space dimensionality and show the successful optimization of a stochastic objective function, enabling identification of probabilistically robust optimal guided weapon designs.

I. Introduction

Guided weapon design often involves designing for a large number of parameters, which are frequently uncertain and often have deeply nonlinear relationships to each other. To enable rapid development of guided weapons, a framework for optimization of candidate designs has been constructed. This framework, called the Multi-Objective Evolutionary Algorithm for the Design of Weapons (MEADoW), which is under active development by CFD Research Corporation, supports rapid design and development of guided weapons by including a variety of robust

---

[1] Intern, CFD Research Corporation, Huntsville, AL;
  M.S. Aeronautics & Astronautics Student, Stanford University, Palo Alto, CA, AIAA Student Member
[2] Research Engineer, CFD Research Corporation, Huntsville, AL

optimization techniques to help efficiently reach an optimal design. The MEADoW framework includes the following optimization methods:

- Single-objective optimization
    - Simulated annealing
    - Particle swarm optimization (PSO)
    - Genetic algorithm
    - Surrogate-assisted genetic algorithm
        - Kriging surrogates
        - Artificial neural network (ANN) surrogates
        - Radial basis functions (RBF)
- Multi-objective optimization
    - Non-dominated sorting genetic algorithm II (NSGA-II)

The genetic algorithms each include several sub-algorithms for the selection, crossover, and mutation operators, and include support for both real and integer design variable constraints.

The MEADoW framework enables fully-automated optimization through its unified, modular design and supports easy selection of design variables, objective functions, optimization approaches, and simulation models, which can be deterministic or stochastic. Additionally, MEADoW can perform rapid optimization using offline and online surrogate modeling in conjunction with the optimization algorithm. Other innovations include development of a new uncertainty metric to prevent stalled optimization, implementation of GPU computing for surrogate model creation, and significant improvements in filtering out bad candidates and efficiently evolving the design population toward an optimal design.

For a given guided weapon design, we must simulate the guided weapon and target engagement scenario and quantitatively assess the quality of the design. We define the variables we want to include in the design space and the objective metric (objective function value, or performance metric) we want to use to compute their performance and then input the design variables and compute the objective metric of the design. The objective metric is often a direct result of simulating the trajectory for the given target engagement scenario, but can be constructed from simulation results if an external metric is preferred.

To identify an optimal design, we must create several design candidates and repeat this process, using the individuals' objective function values to inform the process of incrementally locating the optimal design. Since our objective function is not necessarily differentiable or continuous everywhere, we must use gradient-free optimization approaches. For this, we will use a genetic algorithm, which will generate a population of designs, evaluate the designs, and evolve the design population according to the single- or multi-objective optimization problem.

Most applications of optimization approaches, including gradient-based optimization approaches, use a deterministic objective function. In this paper, we will demonstrate the optimization of designs having a stochastic objective function through the application of a Monte Carlo analysis. The non-determinism in the objective function presents challenges here, since both gradient-based and gradient-free optimization approaches are susceptible to being redirected on a stochastic object. We use the term *general optimum*, $\hat{x}$, to represent the expected value of the argument minimizing the objective function $f(X, x)$, which is a deterministic general function of a vector of random variables, X, and a vector of design variables, x.

$$\hat{x} = E\left[\arg\min_{x} f(X, x)\right]$$

If the effects of the random variables are large (strong stochastic effects), it may not be possible to locate a general optimum, however if the effects of the random variables are small (weak stochastic effects), it may be possible to locate a general optimum. If a general optimum can be located, we can know that the identified optimum is the most robust design since it must also minimize the expectation of the of our general function of X and x:

$$\hat{x} = E\left[\arg\min_{x} f(X, x)\right] = \arg\min_{x} E[f(X, x)]$$

Thus, we will focus on finding an optimum for our stochastic objective function using a gradient-free optimization approach – a genetic algorithm – and demonstrating both its optimality and robustness – using probabilistic analysis of the optimal design and its objective function values.

2

II.   Model Configuration and Baseline Performance

A. Model

The MATLAB missile guidance simulator (Figure 1) is a standard three-loop autopilot that simulates the dynamics of a missile seeker, guidance, and trajectory as it tracks a target. The simulation uses an inertial Earth-fixed reference frame with the x- and y-axes in the horizontal plane and the z-axis pointing down. Due to the z-axis pointing down, the altitude $h = -z$. Plots displayed in this paper show the x-axis on the abscissa and the z-axis on the ordinate, but with the ordinate reversed, so that when viewed, values toward the top of the plots correspond to higher altitudes in the natural sense.
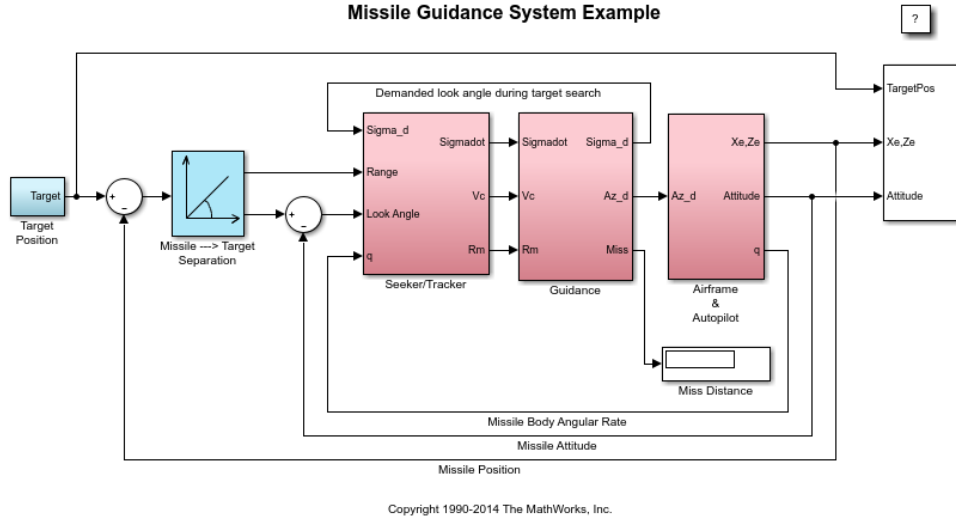
Missile Guidance System Example

Copyright 1990-2014 The MathWorks, Inc.

Figure 1. MATLAB 3-dof missile guidance simulator schematic.

The target is modeled as a two-degree-of-freedom (2-DoF) particle with two translational degrees of freedom in the x- and z-directions. The target is modeled as a purely kinematic particle, that is, with no regard to the forces and moments required to generate the given trajectory. Thus, *any* trajectory can be easily simulated, though only constant velocity (constant magnitude and direction) targets were considered in this experiment.

The missile is modeled as a three-degree-of-freedom (3-DoF) rigid body with two translational degrees of freedom in the x- and z-directions and one rotational degree of freedom about the y-direction. The missile has a body-fixed reference frame, which is equivalent to the standard aircraft reference frame, with the x-axis pointing out the nose, the y-axis pointing out the right side, and the z-axis pointing down (as given by the right-hand rule). The relative orientation of the missile with respect to the inertial Earth-fixed reference frame is tracked using an Euler angle formulation.

Aerodynamics of the missile are computed using table-lookup from an aero model (as a function of angle-of-attack, α, and Mach number, M) along with additional stability and control derivatives, which include pitch damping and the effect of the control actuators on the aerodynamic forces and moments. Atmospheric properties are generated using the International Standard Atmosphere (ISA) model. Thrust is assumed to act through the CG and along the positive body x-axis. Gravity acts along the positive Earth-fixed z-axis. The kinematic evolution equations operate on the Euler angle formulation, providing the necessary information to evolve the vehicle state using the equations of motion:

$$\dot{u} = f_{a_x} + f_t - g\sin\theta - qw \qquad f_x = \frac{F_x}{m} = \frac{QS}{m}C_x = \frac{QS}{m}\left[C_{x_0}(M,\alpha) + C_{x_\delta}\delta\right]; \;\; f_t = \frac{T}{m}$$

$$\dot{w} = f_{a_z} + \qquad g\cos\theta + qu \qquad f_z = \frac{F_z}{m} = \frac{QS}{m}C_z = \frac{QS}{m}\left[C_{z_0}(M,\alpha) + C_{z_\delta}\delta\right]$$

$$\dot{q} = m_a \qquad\qquad\qquad m_a = \frac{\mathcal{M}}{I_{yy}} = \frac{QSD}{I_{yy}}C_m = \frac{QSD}{I_{yy}}\left[C_{m_0}(M,\alpha) + C_{m_q}q + C_{m_\delta}\delta\right]$$

The seeker radar, which has a specified beamwidth, is on a gimbal with gimbal limits and initially scans the field to locate the target – starting by scanning down and then up. Once a target is located, the seeker radar provides

3

estimates of the sightline rate, $\dot{\sigma}$, closing velocity, V_c, and range of the target, R, while a tracking loop and stabilization loop are used to keep the seeker radar pointed at the target while the missile is under guidance. Guidance is established using proportional-navigation guidance with proportional-navigation gain, K, which computes a demanded normal acceleration, a_n^{dem}:

$$a_n^{dem} = KV_c\dot{\sigma}$$

Using the normal acceleration demands, measurements of normal acceleration and body pitch rate from an accelerometer and rate gyro, respectively, and gain-scheduled coefficients as a function of M and α, the demanded normal accelerations are converted into demanded fin actuations. Finally, using a second-order actuator model, the demanded fin actuations, δ^{dem}, are converted into actual fin actuations, δ, which are fed into the equations of motion and used for the aerodynamic force and moment computations. The demanded normal acceleration and demanded fin actuation are subject to saturation and the second-order actuator model enforces the final physical rate and position limits for the actuators.

$$\delta s^2 + 2\zeta\omega_n\delta s + \omega_n^2\delta = \delta^{dem}$$

When the seeker is within a given range of the target, the fuse is activated. When the fuse is activated, if the seeker determines that it is at its closest approach, the fuse is detonated. If no closest approach is detected within 7 seconds, the fuse times out and detonates. At the location of detonation, the range between the missile and target is reported as the miss distance. For targets which are never acquired, no miss distance is reported.

Seeker parameters are listed in Table 1. Normal distributions follow the notation $\mathcal{N}(\mu, \sigma^2)$ and uniform distributions follow the notation $\mathcal{U}(a, b)$. Many of the other parameters in the simulation remained unchanged unless otherwise mentioned. The total simulated time is limited to 20 seconds; integration is controlled using ODE45 with adaptive step size.

Table 1. Seeker Parameter Values

Seeker Parameter	Distribution/Value	Bounds	Units
x_0	0	N/A	m
z_0	-3000	N/A	m
v_0	984 ($M \approx 3.0$)	N/A	m/s
θ_0	0	N/A	rad
q_0	0	N/A	rad/s
m	$\mathcal{N}(204, 3^2)$	$[194, 214]$	kg
I_{yy}	$\mathcal{N}(247, 5^2)$	$[210, 270]$	kg-m^2

Table 2. Atmospheric Reference Parameter Distributions and Bounds

Reference Parameter	Distribution	Bounds	Units
p_0	$\mathcal{N}(101.325, 1^2)$	$[90, 110]$	kPa
ρ_0	$\mathcal{N}(1.225, 0.025^2)$	$[1.125, 1.325]$	kg/m^3
T_0	$\mathcal{N}(288, 10^2)$	$[260, 320]$	K

B. Stochastic Target Parameter Generation

Targets are two-degree-of-freedom point-mass objects and are configured for constant velocity motion. Thus, target initialization requires the assignment of the initial position vector and initial velocity vector. This initialization is accomplished by generating the initial positions, x_0 and z_0, along with the constant speed, v, and the heading angle, θ, with respect to the positive x-axis. However, instead of direct assignment, we will employ the Monte Carlo (MC) method and generate targets by randomly sampling our specified probability distributions. The target parameter values, distributions, and bounds are provided in Table 3. Note, the z_0 distribution does extend to positive values (negative altitudes), but there is no ground constraint in the simulation and z-values affect only the evaluation of the atmospheric properties.

Table 3. Target Parameter Distributions, Values, and Bounds

Target Parameter	Distribution/Value	Bounds	Units
x_0	$\mathcal{N}(9000, 4000^2)$	$(-\infty, \infty)$	m
z_0	$\mathcal{N}(-3000, 3000^2)$	$(-\infty, \infty)$	m
v	$328\ (M \approx 1.0)$	N/A	m/s
θ	$\mathcal{U}(0, 2\pi)$	N/A	rad

For random number generation, we use the Mersenne Twister pseudorandom number generator and provide a random number generator seed so that the target set is reproducible. The reproducibility introduced by random number generator seeding also enforces that for a specific seed, when two different numbers of samples are drawn, that one sample is a strict subset of the other sample. For example, for the same seed, if m samples are drawn to form set A and n samples are drawn to form set B, then $A \subset B \ \forall \ \{m, n\} \mid n > m; \{m, n\} \in \mathbb{Z}$. We will exploit this property in our experiment to demonstrate improved optimal solutions for an increased target space generated using the same seed.

Our stochastic parameter sets (Table 1 and Table 2) for each optimization are generated using random seed 50.

C. Training Data Sets

We use the bivariate normal distribution for the spatial distribution and seed 1 for the random number generation to construct the following 20 MC and 100 MC target sets for training (Figure 2 and Figure 3, respectively). Here, we note that the 20 MC target set is a strict subset of the 100 MC target set and thus the 20 MC targets can be discriminated among the 100 MC targets. The random samples' x- and z-distributions approach normal distributions as the sample size increases. To help visualize the bivariate normal spatial distribution, the 1σ, 2σ, and 3σ ellipses – which correspond to 32%, 5%, and 0.3% exceedance probabilities – are superimposed on the plots.

The polar distribution of targets with respect to the seeker's initial position (using seeker view angle, ψ, not target heading angle, θ) is also depicted in the figures and shows an increasingly smoother distribution as the sample size increases. A majority of the targets are located in $\psi \in [-30°, 30°]$. The polar distribution is not necessarily a normal distribution despite being a composition of two normal distributions. However, since the seeker's initial position is constant, the mean of the target z-distribution is identical to the seeker's initial z position, and the target z-distribution is normal, we expect that the distribution should be symmetric about $\psi = 0°$. This is difficult to see for small sample sizes, but the distribution approaches this symmetry as the sample size increase – especially for the 1,000 and 10,000 sample testing target sets.
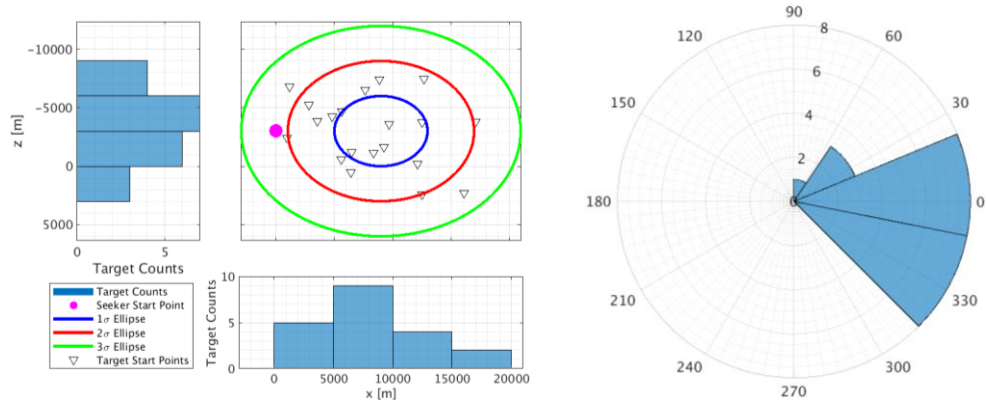
Figure 2. Rectangular (*left*) and polar (*right*) target distributions for the set of 20 training targets.
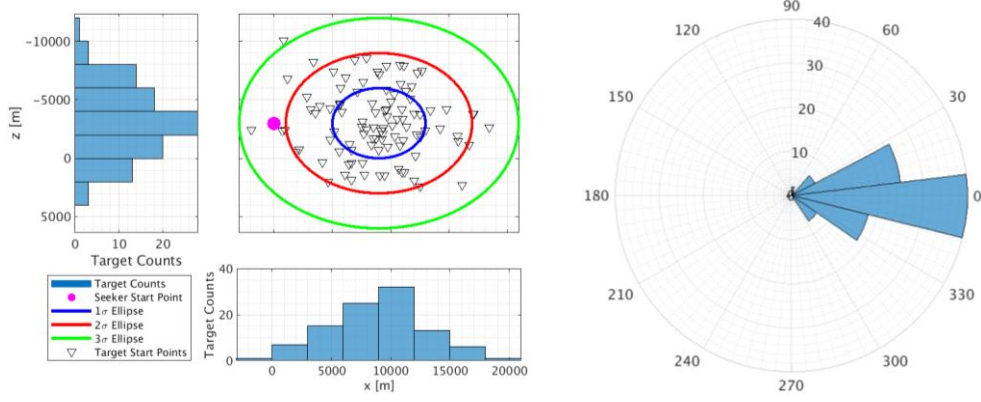
5

Figure 3. Rectangular (*left*) and polar (*right*) target distributions for the set of 100 training targets.

D. Testing Data Sets

We again use the parameter distributions and now use seed 23 for random number generation to construct the following 1,000 MC and 10,000 MC target sets for testing (Figure 4 and Figure 5, respectively). Again, the 1,000 MC target set is a strict subset of the 10,000 MC target set and thus the 1,000 MC targets can be discriminated among the 10,000 MC targets – albeit much more difficult to see. The random samples' x- and z-distributions clearly approach the specified normal distributions and the symmetry of the polar distribution of targets with respect to the seeker's initial position is clearly symmetric about $\psi = 0°$.
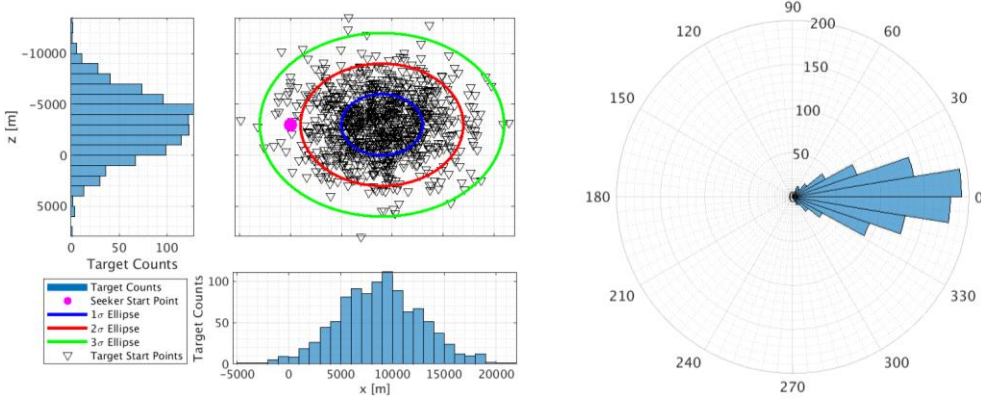
Figure 4. Rectangular (*left*) and polar (*right*) target distributions for the set of 1,000 testing targets.
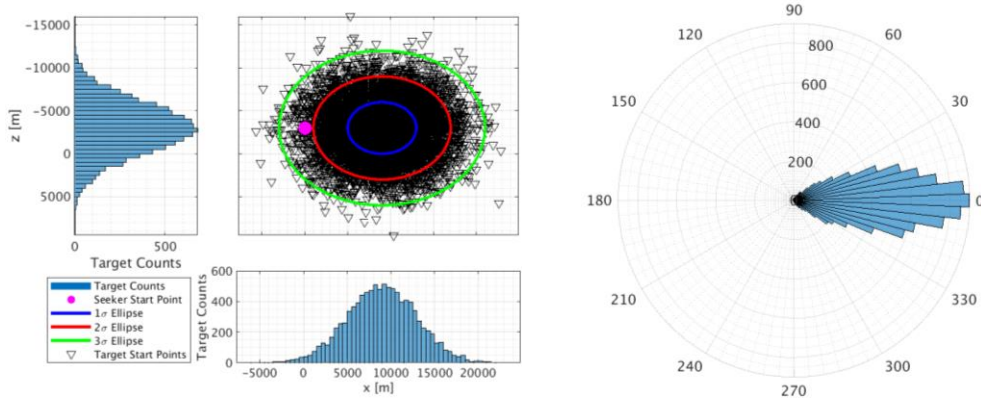

Figure 5. Rectangular (*left*) and polar (*left*) target distributions for the set of 10,000 testing targets.

6

E. Baseline Simulation Parameters

For each case, we will always use the seeker parameter set outlined in Table 1 along with the atmospheric reference parameter set outlined in Table 2. We will test every case using both the 1,000 MC and 10,000 MC target sets generated using distributions and values outlined in Table 3.

.   To establish a baseline performance on which to optimize, we use the baseline simulation parameters listed in Table 4 (which will become design variables to be optimized in other cases).

Table 4. Baseline Simulation Parameters

Parameter Class	Simulation Parameter	Baseline Value	Units
Seeker	Seeker dish gimbal limits	35.0	deg
	Seeker dish beamwidth	20.0	deg
	Maximum normal acceleration	40.0	G
Guidance	Proportional-navigation gain	-3.50	-
	Anti-windup gain	5000	-
	Stabilization gain	40.0π	-

The six simulation parameters encompass two areas, which are labeled *seeker* and *guidance*. The seeker parameters include the seeker dish gimbal limits, seeker dish beamwidth, and maximum normal acceleration; the guidance parameters include the proportional-navigation gain, anti-windup gain, and stabilization gain.

The proportional-navigation gain is the parameter K listed in Section II.A and parameterizes the responsiveness (e.g. fast and undamped, or slow and damped, etc.) of the missile in maintaining a direct hit trajectory due to a non-zero sightline rate. Anti-windup gain is a gain applied on the fin actuator demands to prevent integrator windup, avoid nonlinearity, and improve performance of the fin actuator demands in the presence of a saturated signal (a case where the fin demand is above the maximum demand and thus, is limited to the maximum, even if more control input is applied). The stabilization gain is a proportional gain used to control responsiveness of the seeker dish in response to dish error arising from a moving target, missile body rotation, or other error. The seeker dish gimbal limits are the maximum angles that the seeker dish can pivot to; the seeker dish beamwidth is the range in which targets may be detected. The central axis of the seeker beam coincides with the seeker dish axis. Finally, the maximum normal acceleration is a physical constraint, which is often determined by structural limits. Maximum normal acceleration determines the minimum turning radius ($a_n = v^2/r$; and since the forward speed v is essentially constant, $r_{min} = v^2/a_{n,max}$).

A diagram of the seeker radar (dish, or simply, seeker) is shown in Figure 6. The seeker dish is shown in red and pivots around the missile axis (dashed black line). The seeker dish can pivot between the upper and lower gimbal limits (dotted green lines). The seeker dish has a beamwidth (blue sector/arc) that is centered on the seeker dish axis (dashed red line). To detect targets, the seeker dish pivots between the gimbal limits – targets within the seeker beamwidth are considered detected. Thus, expanding the gimbal limits and seeker beamwidth enables a higher acquisition rate of targets due to a larger accessible field of view (FOV), which is equivalent to the sum of twice the gimbal limit (G_{lim}) and twice the half-beamwidth ($u/2$): $FOV = 2G_{\text{lim}} + 2(u/2)$
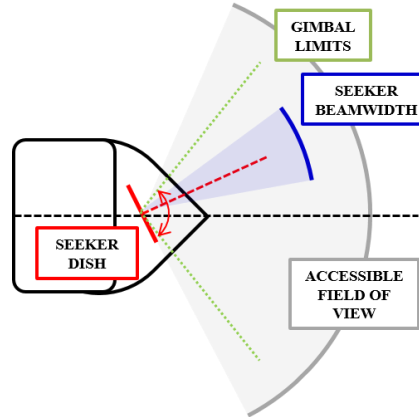
Figure 6. Seeker radar diagram depicting seeker beamwidth, gimbal limits, and total accessible field of view.

III. Optimization

We consider herein, four cases:

- Baseline   (0 design variables; *Baseline* parameters)
- Seeker optimization   (3 design variables; *Seeker* parameters)
- Guidance optimization   (3 design variables; *Guidance* parameters)
- Combined guidance and seeker optimization   (6 design variables; *Guidance* and *Seeker* parameters)
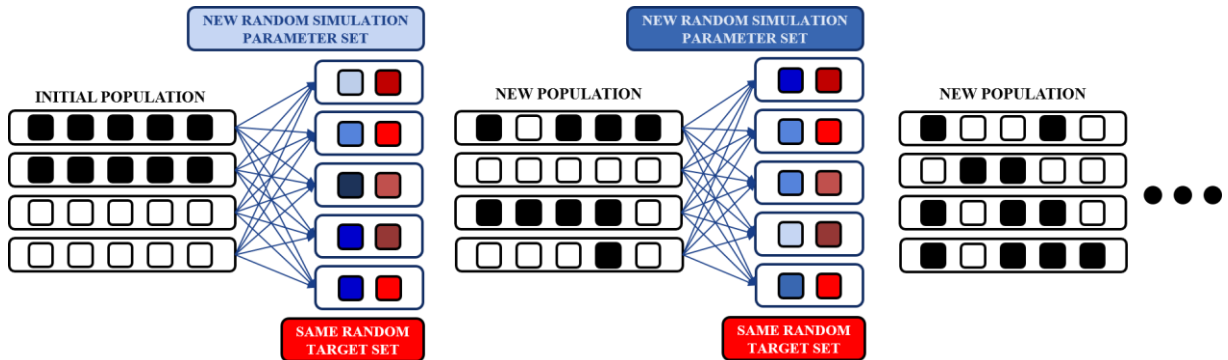
Genetic Algorithm Configuration

The genetic algorithm begins by initializing a population of a specified number of individuals and evaluating their fitness functions. The fitness function is the mean of the miss distances from the Monte Carlo-based objective function evaluations, however, for targets not acquired, the miss distance is now reported as a constant penalty of 50 meters. This penalty on non-acquired targets incentivizes acquisition of targets and is large enough in the mean sense to be comparable to reducing miss distances on already-acquired targets.

Following the fitness function evaluation, the tournament selection operator is applied with a tournament size of 2. After this, the intermediate crossover operator is applied using a crossover fraction of 2 divided by the number of design variables (3 variables: 2/3; 6 variables: 1/3) and a crossover ratio of 1.2. Following this, the Gaussian mutation operator is applied using a mutation fraction of 2 divided by the number of design variables (3 variables: 2/3; 6 variables: 1/3), scale parameter of 0.1, and shrink parameter of 0.5. For each of the newly-created individuals, the fitness function is evaluated and the process repeats with the selection, crossover, mutation, and fitness function evaluation until a stop criterion is met. For this analysis, the stop criterion was chosen to be a generation limit. Tabulations of the population size, generation limit, and number of objective function evaluations for each of the optimization cases are provided in Table 5.

Table 5. Genetic Algorithm Parameters for Each Optimization Case

Number of Design Variables	Number of MC Simulations	Population Size	Generation Limit	Number of Objective Function Evaluations
3	20	40	25	20,000
	100		50	200,000
6	20	60	25	30,000
	100		50	300,000

We make a small modification to the traditional genetic algorithm to enable fair comparison between generations that have different sets of simulation parameters. Traditional genetic algorithms traditionally pool individuals from the previous generation and use the fitness scores for mating pool selection. Since our objective function is non-deterministic, the old population must be re-evaluated with the new set of stochastic parameters and new fitness scores must be computed. This fair metric can now be used to select from the pooled population. In this way, the genetic algorithm population is essentially doubled and selects robust designs which have good fitness scores across generations for multiple simulation parameter sets.

Figure 7. Diagram of the genetic algorithm operating on a generationally-stochastic simulation parameter set and a generationally-deterministic target set.

Included Plots

The plots included are of two types: 1) empirical distribution functions and histograms of the miss distances and 2) trajectory spaces of seeker, targets, and intercepts.

Sample plots of the first type are shown below (Figure 8) – the same plot is depicted in the left and right figures, but on a linear x-scale in the left figure and on a logarithmic x-scale in the right figure. The plots depict two cases: a baseline case (in blue) and an optimized case (in red). In the plost, we see histograms of the 10,000 reported miss distances for the corresponding 10,000 MC simulations. A thinly-dashed line indicates the empirical distribution function (eCDF or EDF) for the 1,000 MC test target set and a lightly-filled region denotes the 95% confidence bounds on this EDF. A heavily-struck line indicates the EDF from the 10,000 MC test target set and a darker-filled, smaller region denotes the 95% confidence bounds on this EDF. The x-axis of the plot is clipped when both distributions have reached a cumulative probability of at least 0.9, which intersects the thick, dashed, black horizontal reference line.

We present these distributions to a cumulative probability of 0.9 since the tail of the distribution is exceptionally long when presented on a linear scale. To further show some of the improvements, we present these plots on both a linear and logarithmic x-scale. Complete EDFs, to a cumulative probability of 1, are included in Appendix A – Complete Miss Distance Distributions on page 22. We also only show the histogram for the 10,000 MC test cases since the histograms for the 1,000 MC test cases have similar trends but less refinement.
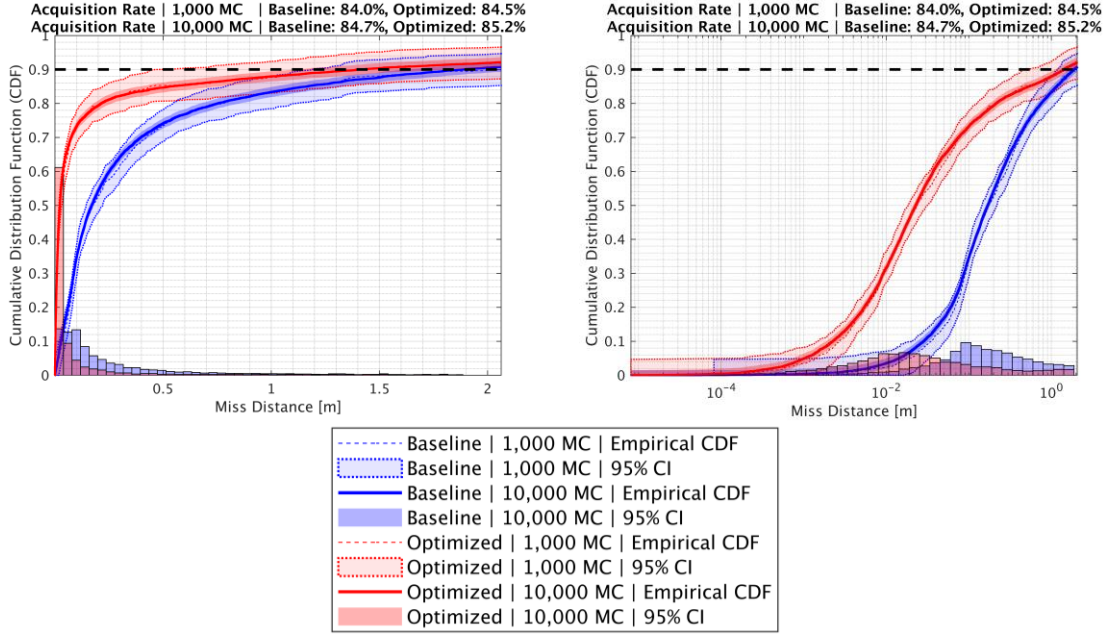
Figure 8. Sample empirical distribution function and histogram plot.

The confidence bounds in the plots are achieved using the Dvoretzky-Kiefer-Wolfowitz (DKW) inequality. We want to state with a given confidence that empirical distribution function we have obtained with some number of samples is within some error of the true, underlying cumulative distribution function. For some natural number of samples, n, we have the true cumulative distribution function $F(x)$, describing the *probability* of a single random variable X being smaller than x and the empirical distribution function $F_n(x)$, describing the *fraction* of random variables smaller than x.

$$F_n(x) = \frac{1}{n}\sum_{i=1}^{n} \mathbf{1}_{\{X_i \le x\}} \qquad \forall\, x \in \mathbb{R}$$

The DKW inequality states that for these real-valued independent and identically distributed random variables, there is a bound on the probability of the absolute error between our empirical distribution function and the true cumulative distribution function, F_n and F, differing by more than a given constant ε.

9

$$\Pr\left(\sup_{x\in\mathbb{R}}|F_n(x) - F(x)| > \varepsilon\right) \leq 2e^{-2n\varepsilon^2} \qquad \forall\, \varepsilon > 0$$

It also states that this probability bound is governed by the number of samples, n, and the constant ε, which is defined for probability of $1 - \alpha$:

$$\varepsilon = \sqrt{\frac{1}{2n}\ln\frac{2}{\alpha}}$$

Thus, we can construct bounds containing the true underlying CDF with confidence (probability) $1 - \alpha$ as an upper bound, $U(x)$, and a lower bound, $L(x)$ as follows:

$$U(x) = \min(F_n(x) + \varepsilon, 1)$$
$$L(x) = \max(F_n(x) - \varepsilon, 0)$$

$$L(x) \leq F(x) \leq U(x)$$

For our case, the responses from the objective function are *independent* since the output of one function evaluation does not correlate to the input of another function evaluation and *identically-distributed* since they responses belong to the same underlying distribution (process) which governs the objective function. Thus, since the objective function is independent and identically distributed, the DKW confidence limits converge to the true CDF in the limit of infinite samples. So, we can construct bounds around our empirical distribution functions for a given number of samples and we can state with specified confidence levels that the true CDF is contained within the bounds.

A sample plot of the second type is shown below (Figure 9). The plot on the left and right are identical and have equal axis scaling, but the left figure is shown in inertial rectangular coordinates and the right figure is shown in seeker-relative polar coordinates to help demonstrate range and field of view.

The initial position of the seeker is depicted as a large magenta circle and the seeker is initially traveling directly to the right in the plot. The initial position of targets that were acquired are depicted as blue, green, and yellow triangles and the initial location of targets that were not acquired are depicted as red triangles. The locations of intercept are depicted as blue, green, and yellow x-s, corresponding to the color of the target. Two boundaries are drawn: a blue boundary around the space of all acquired targets and a black boundary around the space of all intercepts. The boundaries are drawn using MATLAB's boundary function with a shrink factor of 0.5. In all plots, the boundaries are not perfectly symmetric around the seeker due to the initial target acquisition algorithm that commands the seeker dish to pivot down and then up.
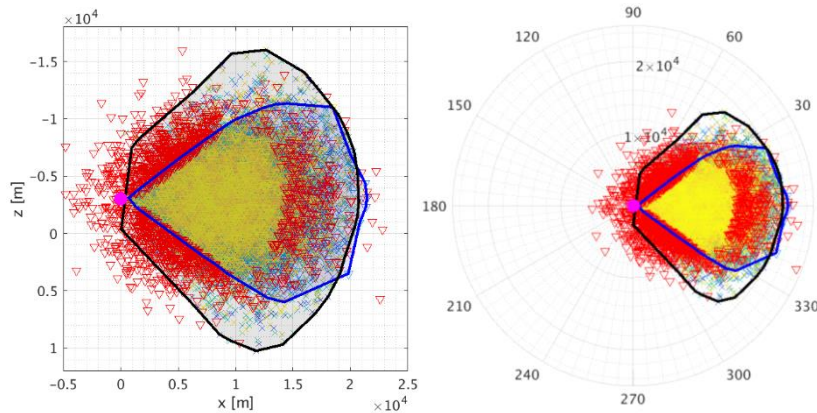
Figure 9. Sample intercept space plot for the 10,000 MC target set.

We note here that the 10,000 MC target space is well-defined and although we will use the areas of the intercept spaces for the 1,000 MC and 10,000 MC simulations as a metric, we will not show the 1,000 MC plots in our discussion since they are often less-well-defined and still visually similar to the 10,000 MC plots. The 1,000 MC plots are included in Appendix B – 1,000 MC Testing Target Set Trajectories on page 23.

A. Baseline Performance

The results of the 10,000 MC testing target set baseline simulation are shown in Figure 10. We observe a roughly 70-degree field of view and roughly 120-degree field of intercept. The baseline acquisition rate for the 10,000 MC testing target set simulation is 84.7% *for the given distribution of targets*. Targets outside of the field of view are simply unseen and some targets beyond 10 km cannot be reached in the 20 seconds of simulation time, so we note a limit on the radial distance of targets able to be intercepted.
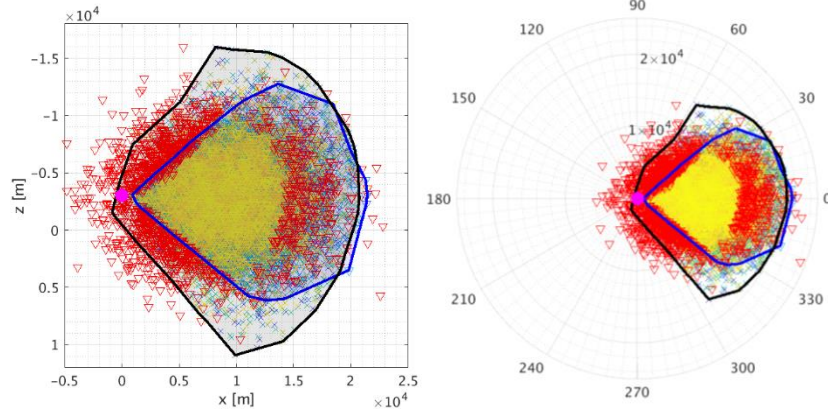
Figure 10. Rectangular (*left*) and polar (*right*) trajectory spaces for the baseline case tested with the 10,000 MC target set.

Table 6. Acquisition Rates, Target Areas, and Intercept Areas for the Baseline Case

Training Set	Baseline		Units
Testing Set	*1,000 MC*	*10,000 MC*	
Acquisition Rate	84.0	**84.7**	%
Target Space	216.0	**249.5**	km^2
Intercept Space	347.1	**389.5**	km^2

B. Seeker Optimization

In this case, we set the seeker dish gimbal limits, seeker dish beamwidth, and maximum normal acceleration as the design variables; the bounds on the three design variables are listed in Table 7. The configuration of the genetic algorithm corresponds to the *three-design variable* row in Table 5. We expect that the optimization of seeker parameters should lead to an improved miss distance distribution and greatly improved target acquisition though only because of the design variables being optimized, since the objective remains a minimization of miss distance. Additionally, we expect the 100 MC training target set case to yield a better optimum over the 20 MC training target set case due to a larger sample size and longer training time.
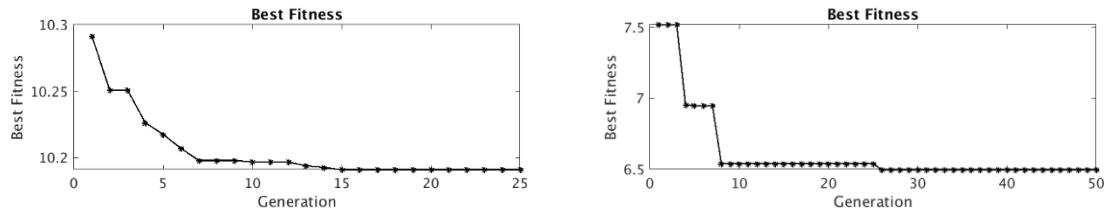

Figure 11. Convergence of the stochastic fitness function to optimal solutions for the optimized seeker case trained with the 20 MC target set (*left*) and the 100 MC target set (*right*).

The genetic algorithms both improved the best fitness score, though the 100 MC training target set found better improvement during training that led to a better overall fitness score *for that target set*. We observe convergence of the genetic algorithm on the stochastic objective function (Figure 11).

11

For the 20 MC training target set, we see improved miss distance performance – at the 1,000 MC testing target set, there is enough uncertainty that we cannot be certain that the miss distance distributions have improved, however, the 10,000 MC testing target set tightens the bounds around the updated distributions and demonstrates a small improvement over the baseline (Figure 12). The acquisition rate for the 20 MC training target set is below the baseline performance, likely due to the arrangement of the targets not necessitating large fields-of-view.

For the 100 MC training target set, we see similar miss distance distribution performance, with the 1,000 MC testing target set having enough uncertainty not to claim great improvement, but those bounds are again tightened in the 10,000 MC testing target set and show a small improvement (Figure 13). On the other hand, we see quite a strong improvement in the target acquisition rate to 89.2% over the baseline's 84.7%. We attribute this to a larger sample size in the target set that offers fitness benefits to individuals that have larger fields of view and can acquire more targets while maintaining good miss distance performance.
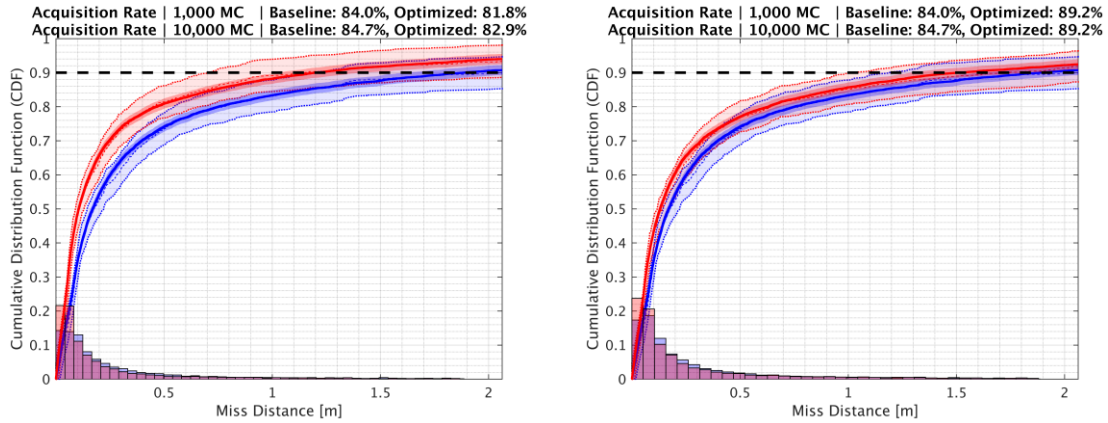

Figure 12. Empirical distribution functions and histograms on a linear x-scale for the baseline case (*blue*) and optimized seeker case (*red*) trained with the 20 MC (*left*) and 100 MC (*right*) target sets.
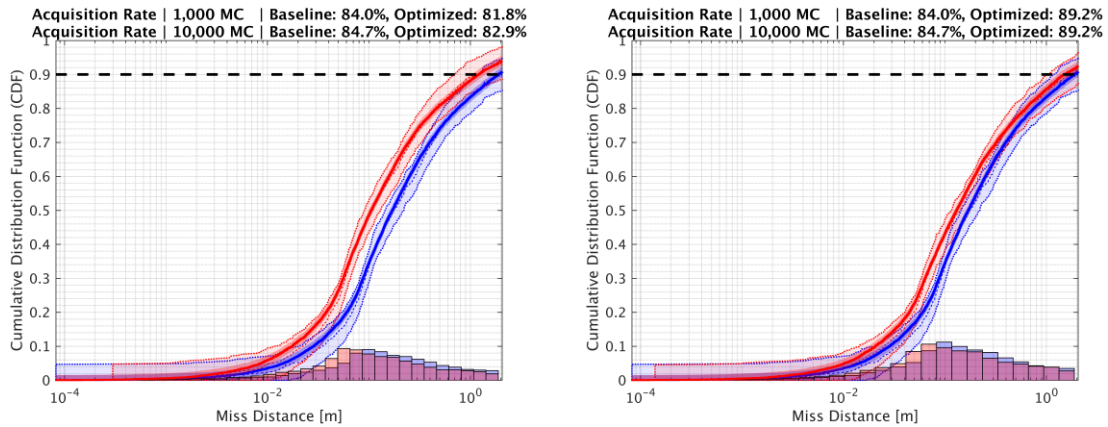

Figure 13. Empirical distribution functions and histograms on a logarithmic x-scale for the baseline case (*blue*) and optimized seeker case (*red*) trained with the 20 MC (*left*) and 100 MC (*right*) target sets.

The difference in the acquisition rates between the 20 MC and 100 MC training target sets is especially apparent in the trajectory space plots depicted in Figure 14 and Figure 15. The target space spans only about 60 degrees in the 20 MC training target set case, but is expanded to over 90 degrees in the 100 MC training target set case. In addition, the 100 MC training target set case shows that some intercepts are possible nearly perpendicular to the seeker's initial velocity. We also see the first nuance of the "down-then-up" scanning of the seeker during the target acquisition phase in the 100 MC trajectory space plot where there are a number of targets on the upper half of the target space that seem to infringe on the no-escape zone, but likely escape due to the scanning behavior.
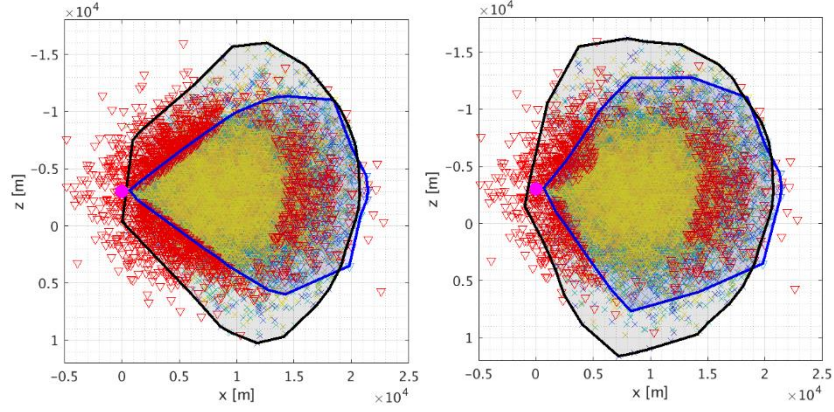
Figure 14. Rectangular trajectory spaces for the optimized seeker case trained with the 20 MC (*left*) and 100 MC (*right*) target sets and tested with the 10,000 MC target set.
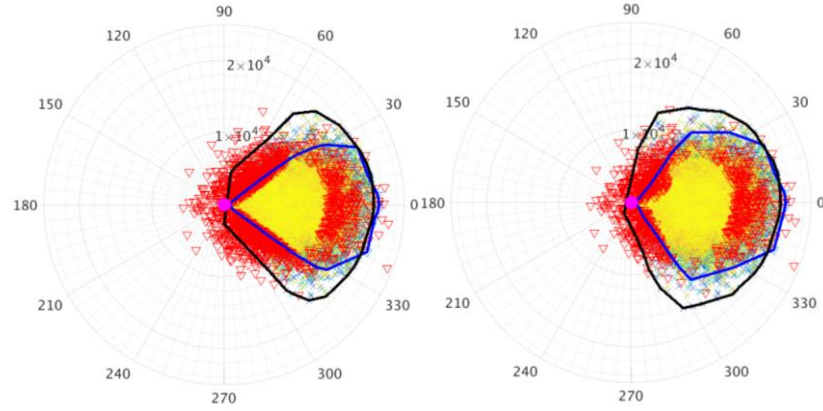
Figure 15. Polar trajectory spaces for the optimized seeker case trained with the 20 MC (*left*) and 100 MC (*right*) target sets and tested with the 10,000 MC target set.

The baseline and optimal designs for this case are included in Table 7. The optimal designs frequently maximized nearly all the included design variables, but did not necessarily identify the bounds as the global optimum. It is this example that reminds us that there are often subtle trade-offs that affect performance in these highly nonlinear problems. For example, while having the largest possible maximum normal acceleration minimizes turning radius and thus making turning easier thereby expanding the accessible intercept space, having a large normal acceleration limit might lead to overshoot in the terminal phase of the trajectory, creating error in the final miss distance.

Overall, we see a small improvement in the miss distance distributions, a great improvement in the acquisition rate, and some great expansions of the target and intercept spaces over our baseline for our 100 MC training target set and 10,000 MC testing target set (Table 8).

**Table 7. Baseline and Optimal Individuals for the Optimized Seeker Case**

Parameters	Baseline Individual	Optimal Individual (20 MC)	Optimal Individual (100 MC)	Optimization Bounds	Units
Seeker dish gimbal limits	35.0	29.1	50.0	[20.0, 50.0]	deg
Seeker dish beamwidth	10.0	15.0	14.3	[5.0, 15.0]	deg
Maximum normal acceleration	40.0	57.3	56.8	[20.0, 60.0]	G
Proportional-navigation gain	-3.50	-3.50	-3.50	-	-
Anti-windup gain	5000	5000	5000	-	-
Stabilization gain	40.0π	40.0π	40.0π	-	-

13

Table 8. Acquisition Rates, Target Areas, and Intercept Areas for the Optimized Seeker Case

Training Set	Baseline		20 MC Target Set		100 MC Target Set		Units
Testing Set	*1,000 MC*	*10,000 MC*	*1,000 MC*	*10,000 MC*	*1,000 MC*	*10,000 MC*	
Acquisition Rate	84.0	**84.7**	81.8	**82.9**	89.2	**89.2**	%
Target Space	216.0	**249.5**	193.9	**230.8**	252.7	**297.4**	km^2
Intercept Space	347.1	**389.5**	315.6	**378.7**	406.4	**450.2**	km^2

C. Guidance Optimization

In this case, we set the proportional-navigation gain, anti-windup gain, and gimbal stabilization gain as the design variables; the bounds on the three design variables are listed in Table 9. The configuration of the genetic algorithm corresponds to the *three-design variable* row in Table 5. We expect that the optimization of guidance parameters will lead to an improved miss distance distribution, but not necessarily other metrics related to target acquisition, such as acquisition rate and target space areas. Additionally, we expect the 100 MC target set case to yield a better optimum over the 20 MC target set case due to a larger sample size and longer training time.
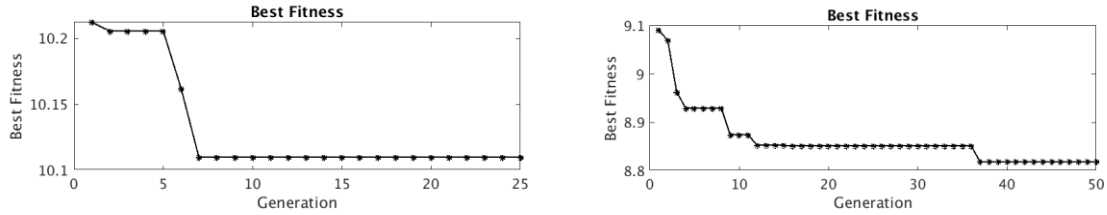

Figure 16. Convergence of the stochastic fitness function to optimal solutions for the optimized guidance case trained with the 20 MC target set (*left*) and the 100 MC target set (*right*).

The genetic algorithms both improved on the best fitness score, though again, the 100 MC training target set case found better improvement during training that led to a better overall fitness score *for that target set*. We observe convergence of the genetic algorithm on the stochastic objective function (Figure 16).

For the 20 MC training target set in Figure 17, we note a great improvement in miss distance distributions even for the 1,000 MC testing target set. The EDFs are clouded with some uncertainty in the low- and high-order log regions that is easily resolved by the 10,000 MC testing target set. The guidance parameters clearly have much more impact on the miss distance than the seeker parameters. On the other hand, we note that the acquisition rates are essentially identical to those of the baseline case.

For the 100 MC training target set in Figure 18, we see similar miss distance distribution performance, with the 10,000 MC testing target set removing the uncertainty of the 1,000 MC testing target set and demonstrating good improvement over the baseline.
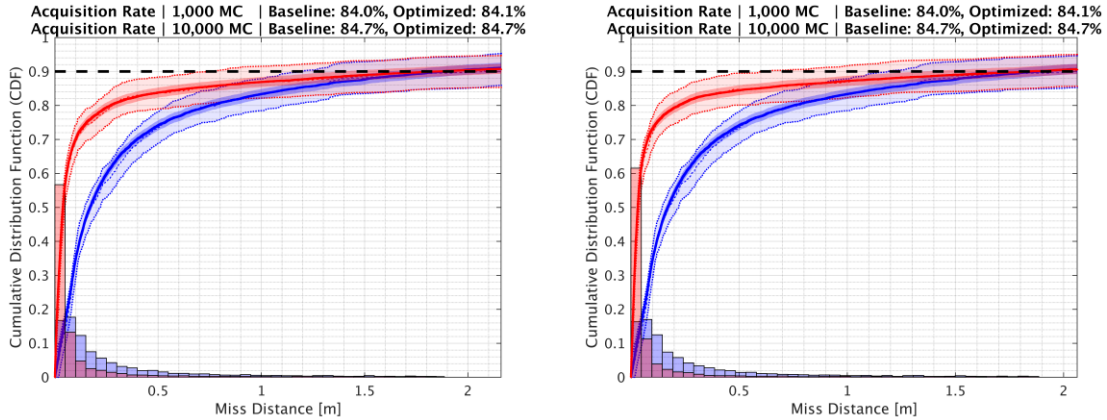

Figure 17. Empirical distribution functions and histograms on a linear x-scale for the baseline case (*blue*) and optimized guidance case (*red*) trained with the 20 MC (*left*) and 100 MC (*right*) target sets.

14
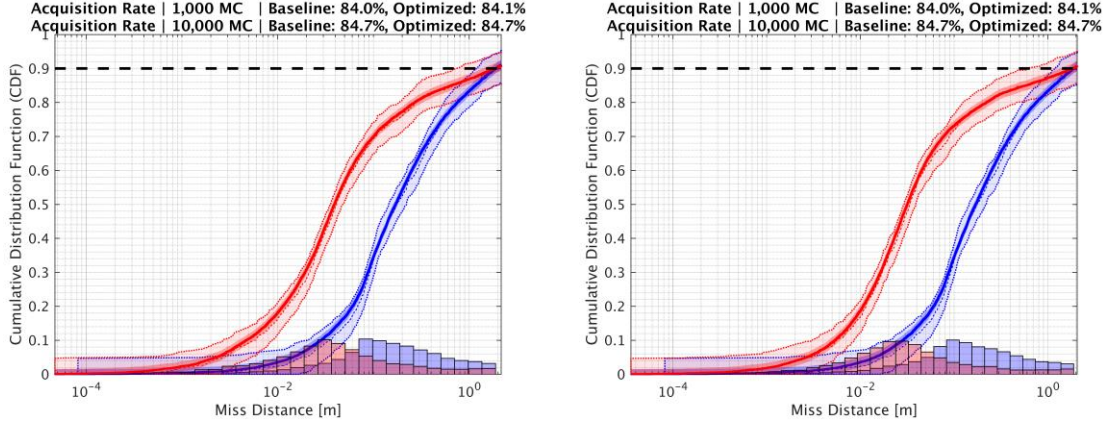
Figure 18. Empirical distribution functions and histograms on a logarithmic x-scale for the baseline case (*blue*) and optimized guidance case (*red*) trained with the 20 MC (*left*) and 100 MC (*right*) target sets.

The trajectory space plots (Figure 19 and Figure 20) are not too informative, as the acquisition rates were nearly identical and the major improvement in the miss distances was on the order of 10-100 cm.
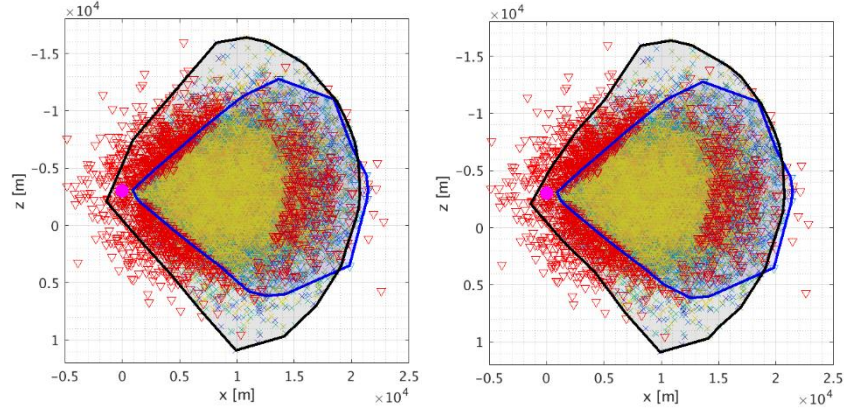
Figure 19. Rectangular trajectory spaces for the optimized guidance case trained with the 20 MC (*left*) and 100 MC (*right*) target sets and tested with the 10,000 MC target set.
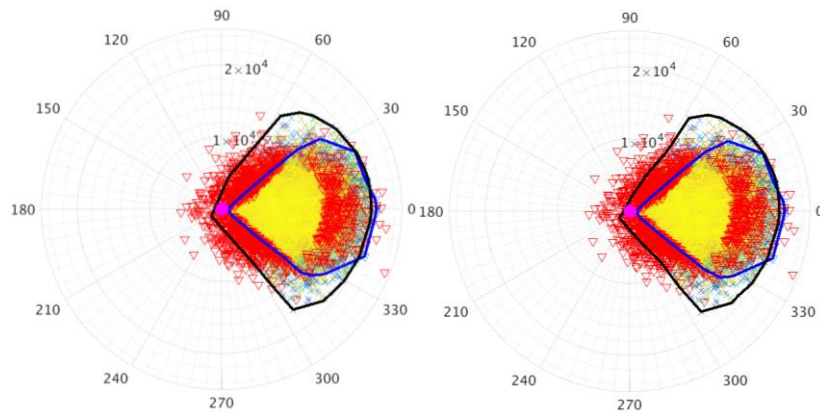
Figure 20. Polar trajectory spaces for the optimized guidance case trained with the 20 MC (*left*) and 100 MC (*right*) target sets and tested with the 10,000 MC target set.

The baseline and optimal designs for this case are included in Table 9. Unlike the seeker optimization case, the identified optimum for this case did not lie close to any of the bounds. We observe some slight changes in the

15

proportional-navigation gain and some larger changes for the anti-windup gain and stabilization gain. The nonlinear trade-offs here are evidenced in the *seemingly* random optimum that produces greatly-optimized miss distance empirical distribution functions, but little to no change in the acquisition rate or other acquisition-based metrics (Table 10). This is unsurprising since the objective function is still only the miss distance, so any improvements in the acquisition rates is a byproduct of the miss distance optimization.

Table 9. Baseline and Optimal Individuals for the Optimized Guidance Case

Parameters	Baseline Individual	Optimal Individual (20 MC)	Optimal Individual (100 MC)	Optimization Bounds	Units
Seeker dish gimbal limits	35.0	35.0	35.0	-	deg
Seeker dish beamwidth	10.0	10.0	10.0	-	deg
Maximum normal acceleration	40.0	40.0	40.0	-	G
Proportional-navigation gain	-3.50	-3.89	-4.04	[-7.00, -1.00]	-
Anti-windup gain	5000	9944	31363	[500, 50000]	-
Stabilization gain	40.0π	72.7π	87.7π	$[10.0\pi, 160.0\pi]$	-

**Table 10. Acquisition Rates, Target Areas, and Intercept Areas for the Optimized Guidance Case**

Training Set	Baseline		20 MC Target Set		100 MC Target Set		Units
Testing Set	*1,000 MC*	*10,000 MC*	*1,000 MC*	*10,000 MC*	*1,000 MC*	*10,000 MC*	
Acquisition Rate	84.0	**84.7**	84.1	**84.7**	84.1	**84.7**	%
Target Space	216.0	**249.5**	216.0	**249.0**	216.0	**248.4**	km^2
Intercept Space	347.1	**389.5**	346.4	**398.3**	346.6	**389.7**	km^2

D. Guidance & Seeker Optimization

In this case, we set the proportional-navigation gain, anti-windup gain, gimbal stabilization gain, seeker dish gimbal limits, seeker dish beamwidth, and maximum normal acceleration as the design variables; the bounds on the six design variables are listed in Table 11.

The configuration of the genetic algorithm corresponds to the *six-design variable* row in Table 5. Since the design space is much larger, the population size is increased to 60 individuals.

We expect that the optimization of the guidance and seeker parameters together will yield an improved miss distance distribution and simultaneously improved target acquisition. However, we do not expect that the optimum in this combined design space will be equal to the direct vector sum of the optima from each of the other design subspaces since there may be interaction between the design variables not present in each of the design subspaces. Additionally, we expect the 100 MC target set case to yield a better optimum over the 20 MC target set case due to a larger sample size and longer training time.
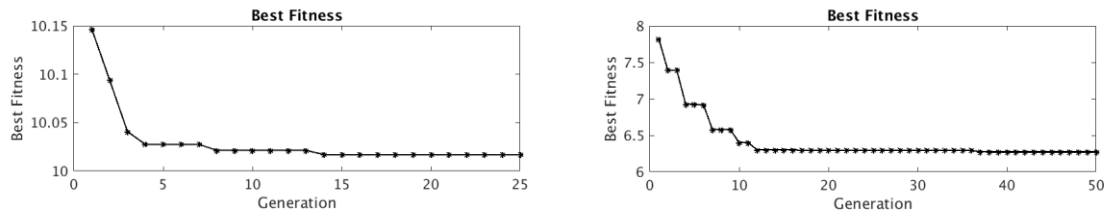

Figure 21. Convergence of the stochastic fitness function to optimal solutions for the optimized guidance and seeker case trained with the 20 MC target set (*left*) and the 100 MC target set (*right*).

The genetic algorithms both improved the best fitness score, though the 100 MC training target set case found better improvement during training that led to a better overall fitness score *for that target set*. We observe convergence of the genetic algorithm on the stochastic objective function (Figure 21).

In Figure 22, for the 20 MC training target set, we see similar miss distance performance to the optimized guidance case, but unlike that case, we see a slight improvement in the acquisition rate over the baseline. The 1,000 MC testing target set EDFs are clouded with some uncertainty in the low- and high-order log regions that is easily resolved by the 10,000 MC testing target set. Again, we note that the minimal improvements in acquisition rate for the 20 MC case

16

over the baseline performance is likely due to the arrangement of the small number of targets not necessitating a large field of view.

For the 100 MC training target set, which is depicted in Figure 23, we see little improvement in the miss distance empirical distribution functions over the 20 MC training target set, but a good increase in the acquisition rate: up to 89.4% over the 20 MC training target set acquisition rate of 85.2% and the baseline acquisition rate of 84.7%.
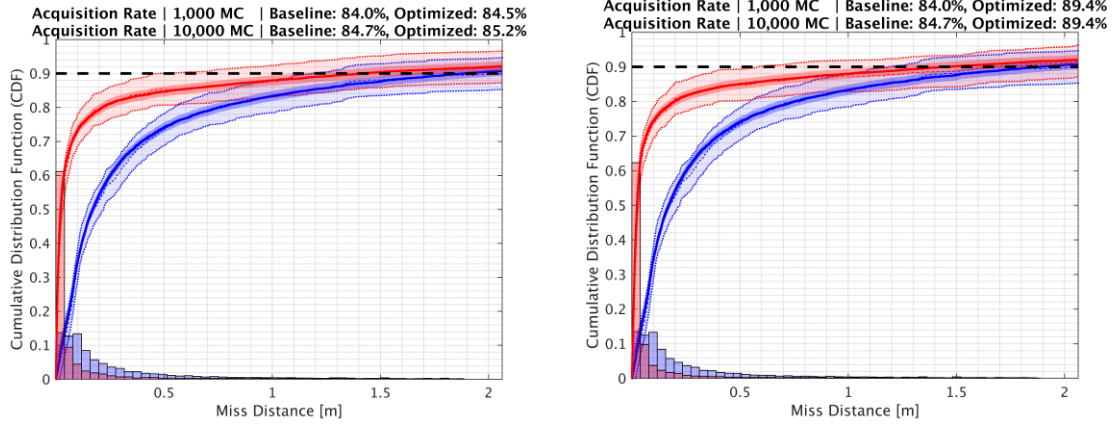

Figure 22. Empirical distribution functions and histograms on a linear x-scale for the baseline case (*blue*) and optimized guidance and seeker case (*red*) trained with the 20 MC (*left*) and 100 MC (*right*) target sets.
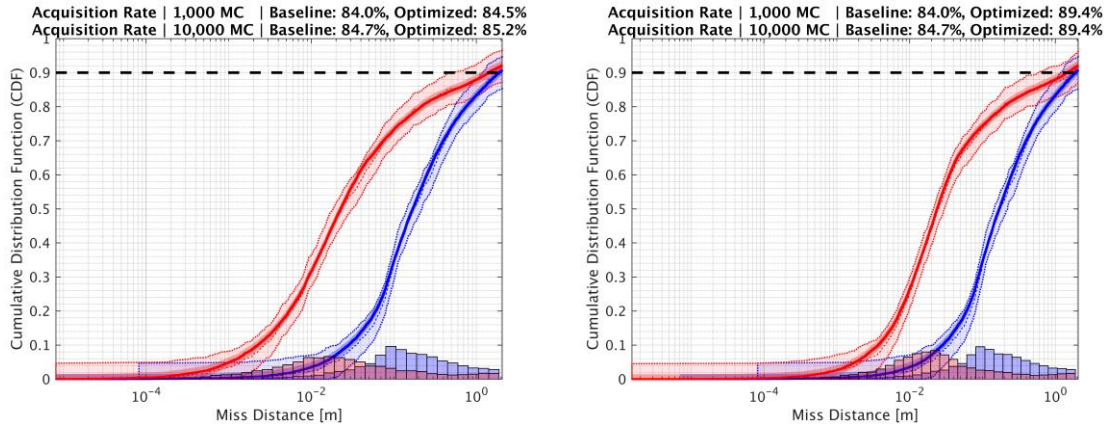

Figure 23. Empirical distribution functions and histograms on a logarithmic x-scale for the baseline case (*blue*) and optimized guidance and seeker case (*red*) trained with the 20 MC (*left*) and 100 MC (*right*) target sets.

The combined guidance and seeker optimization yields significant target space improvement, which can be seen in Figure 24 and Figure 25. For comparison, the baseline field of view is 80 degrees, the seeker-optimized field of view is 115 degrees, the guidance-optimized field of view is 80 degrees, and the guidance-and-seeker-optimized field of view is 115 degrees. There is good improvement demonstrated between the 20 MC training target set and the 100 MC training target set – an enlarged field of view, higher acquisition rate, and maintained improved miss distance distributions. We again see the "down-then-up" scanning pattern of the seeker during the target acquisition phase in the 100 MC trajectory space plot.
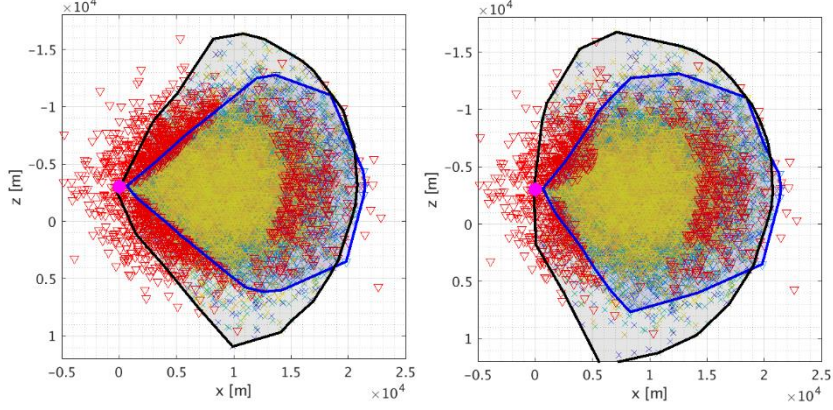
Figure 24. Rectangular trajectory spaces for the optimized guidance and seeker case trained with the 20 MC (*left*) and 100 MC (*right*) target sets and tested with the 10,000 MC target set.
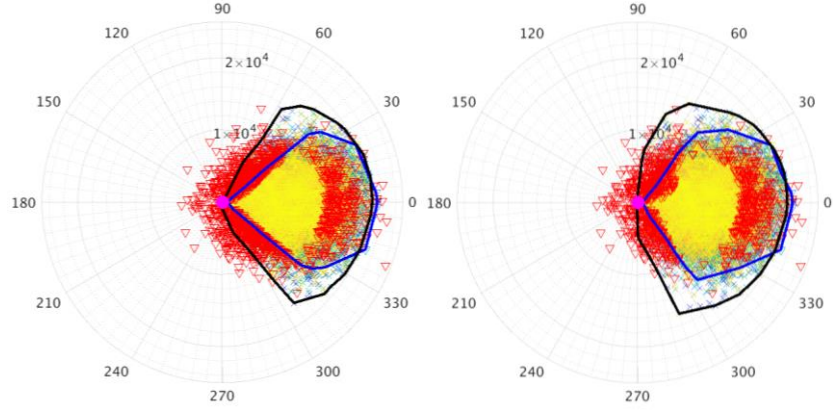
Figure 25. Polar trajectory spaces for the optimized guidance and seeker case trained with the 20 MC (*left*) and 100 MC (*right*) target sets and tested with the 10,000 MC target set.

The baseline and optimal designs for the guidance and seeker optimization are provided in Table 11 and the results of the baseline and optimal designs for the 1,000 MC testing target set and the 10,000 MC testing target set are included in Table 12. We see arguably the biggest difference between baseline, 20 MC, and 100 MC training target sets than we see in any other case. This is likely due to the increased dimensionality of the design space, which cannot be explored as much given the same amount of time and candidate designs. Here, we note that the optimum is located close to the bounds of three of the design space dimensions, but not close to the bounds for three other dimensions.

The combined optimization of both seeker and guidance parameters produced both greatly improved miss distance empirical distribution function performance and greatly improved target spaces and acquisition rates. These acquisition metrics improving is merely a byproduct of the optimal candidate that was obtained only by minimizing a miss-distance-based objective function. As a result of the stochastic Monte Carlo analysis, the identified optimal guided weapon designs are guaranteed to be robust and reach minimum miss distances for simulation and target parameter distributions that match the specified distributions outlined in Table 1, Table 2, and Table 3.

18

Table 11. Baseline and Optimal Individuals for the Optimized Guidance and Seeker Case

Parameters	Baseline Individual	Optimal Individual (20 MC)	Optimal Individual (100 MC)	Optimization Bounds	Units
Seeker dish gimbal limits	35.0	34.0	50.0	[20.0, 50.0]	deg
Seeker dish beamwidth	10.0	15.0	14.3	[5.0, 15.0]	deg
Maximum normal acceleration	40.0	56.7	56.8	[20.0, 60.0]	G
Proportional-navigation gain	-3.50	-4.39	-4.08	[-7.00, -1.00]	-
Anti-windup gain	5000	43852	31465	[500, 50000]	-
Stabilization gain	40.0π	88.7π	115.8π	[10.0π, 160.0π]	-

Table 12. Acquisition Rates, Target Areas, and Intercept Areas for the Optimized Guidance and Seeker Case

Training Set	Baseline		20 MC Target Set		100 MC Target Set		Units
Testing Set	*1,000 MC*	*10,000 MC*	*1,000 MC*	*10,000 MC*	*1,000 MC*	*10,000 MC*	
Acquisition Rate	84.0	**84.7**	84.5	**85.2**	89.4	**89.4**	%
Target Space	216.0	**249.5**	216.1	**251.9**	252.7	**298.2**	km^2
Intercept Space	347.1	**389.5**	326.1	**383.5**	395.7	**456.0**	km^2

IV. Conclusion

All the optimal candidates from the baseline and three optimization cases are tabulated below. Principally, we have demonstrated the convergence of our evolutionary algorithm on a stochastic objective function and have identified optimal guided weapon designs on design spaces of varying dimensionality. However, we have also demonstrated for the combined six-parameter design space that the optimal solution is not necessarily a superposition of the optimal solutions from lower-order design spaces. Considering the 100 MC optimal seeker candidate (S 100), the 100 MC optimal guidance candidate (G 100), and the 100 MC optimal guidance and seeker candidate (GS 100), we observe three things: 1) essentially no variations on the seeker dish gimbal limits, seeker dish beamwidth, and maximum normal acceleration, 2) slight variations on the proportional-navigation and anti-windup gains, and 3) significant variation on the stabilization gain. This highlights the necessity of locating an optimum in high-dimensional design spaces where possible to obtain the most optimal design rather than performing optimizations in reduced design spaces, even if the reduced design spaces are believed to largely independent.

Table 13. All Optimal Candidates (*S: Seeker Optimization; G: Guidance Optimization; GS: Guidance & Seeker Optimization; Number of Targets in Training MC Set; Baseline Parameters Shaded Gray*)

Parameters	B	S 20	S 100	G 20	G 100	GS 20	GS 100	Optimization Bounds	Units
Seeker dish gimbal limits	35.0	29.1	50.0	35.0	35.0	34.0	50.0	[20.0, 50.0]	deg
Seeker dish beamwidth	10.0	15.0	14.3	10.0	10.0	15.0	14.3	[5.0, 15.0]	deg
Max. normal acceleration	40.0	57.3	56.8	40.0	40.0	56.7	56.8	[20.0, 60.0]	G
Pronav. gain	-3.50	-3.50	-3.50	-3.89	-4.04	-4.39	-4.08	[-7.00, -1.00]	-
Anti-windup gain	5000	5000	5000	9944	31363	43852	31465	[500, 50000]	-
Stabilization gain	40.0π	40.0π	40.0π	72.7π	87.7π	88.7π	115.8π	$[10.0\pi, 160.0\pi]$	-

In some cases, we see that employing a probabilistic approach such as the Monte Carlo method can often lead to additional simulation cost due to the order of magnitude of simulations that need to be run in order to have confidence in an improved solution. We demonstrated that this simulation cost could be reduced by introducing additional probabilistic metrics such as the Dvoretzky-Kiefer-Wolfowitz confidence bands for our optimal design's miss distance empirical distribution functions. For some of the cases, the 1,000 MC testing target set demonstrated such a great improvement in the empirical distribution function with 95% confidence bands that further testing was essentially unnecessary. While the DKW confidence bands are merely a tool for estimating the probability of a bounded region containing the true CDF, they can be a good tool for demonstrating convergence, and where appropriate, a good tool for deciding that no further refinement is reasonable for the increased simulation cost.

For example, in cases where the 1,000 MC testing target set with 95% confidence bounds showed no overlap between the baseline and optimized cases (Figure 23), a 10,000 MC testing target set simulation is unnecessary to essentially guarantee improvement. A quick calculation that the true miss distance CDF of the baseline case exceeded the left (upper) bound and that the true miss distance CDF of the optimized case exceeded the right (lower) bound reveals that the probability of such an event occurring is less than or equal to 0.025*0.025 = 0.000625, or less than 7 in 10,000 chance. This chance describes only that the true CDFs are located *at* the bounds and do not exceed them, so the probability that the true CDFs are even further beyond these bounds and possibly even that the optimized model reduces performance, is many orders of magnitude lower. Of course, for more accurate information, we must run more samples, but introducing the DKW-bounded performance ensures that improvement is at least guaranteed with *reasonable* certainty – saving us resources running larger simulations.

Another interesting result is that the performance of the 20 MC training target runs was at best a small improvement, or at worst, a slight deterioration when compared the baseline. It is worth mentioning that a large sample size may be necessary to locate a general optimum depending on the strength of the effects of the random variables and the shape of the expected value of the function.

In all cases, the objective was minimized – all miss distance distributions were better than the baseline model performance. There was minimal improvement in the low- and high-order log range, but in the moderate log range

($\sim 10^{-2}$ to 10^{-1}), the empirical distribution functions could be improved by nearly an order of magnitude. Since we could only optimize this middle range, we suggest using a logarithmic miss distance-based objective, to help reduce the extremity of values and normalize the optimization behavior across multiple orders of magnitude. Additional extensions of this work could include accelerating, maneuvering targets and single- or multi-objective optimization with surrogate assistance.

V. Appendix A – Complete Miss Distance Distributions
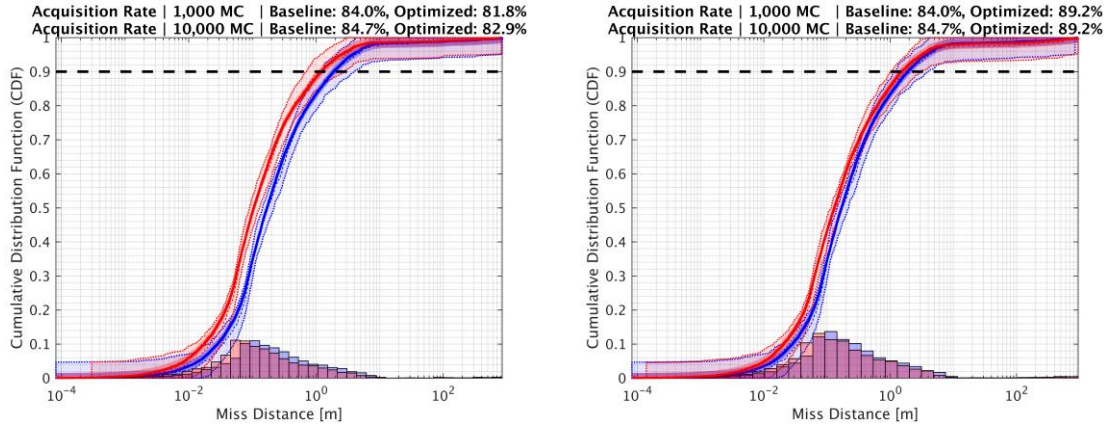
Figure 26. Empirical distribution functions and histograms for the baseline case (*blue*) and optimized seeker case (*red*) trained with the 20 MC target set (*left*) or the 100 MC target set (*right*).
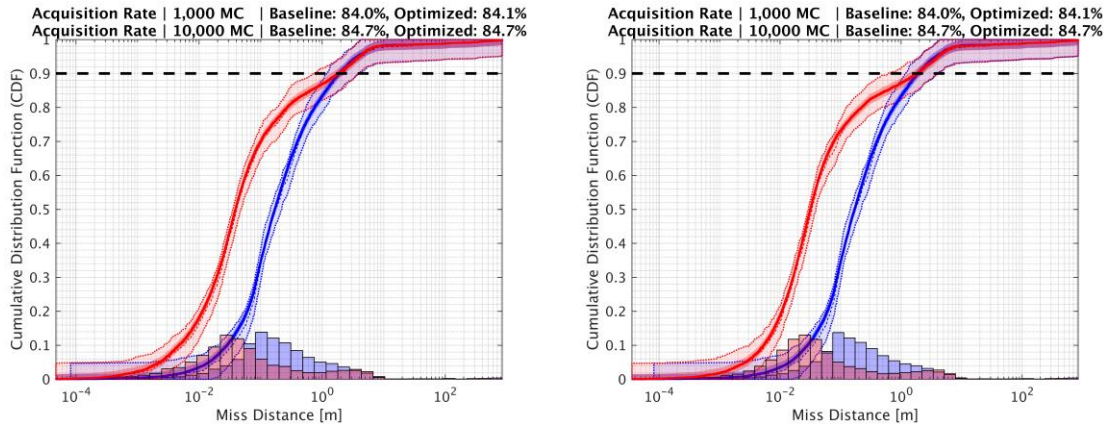
Figure 27. Empirical distribution functions and histograms for the baseline case (*blue*) and optimized guidance case (*red*) trained with the 20 MC target set (*left*) or the 100 MC target set (*right*).
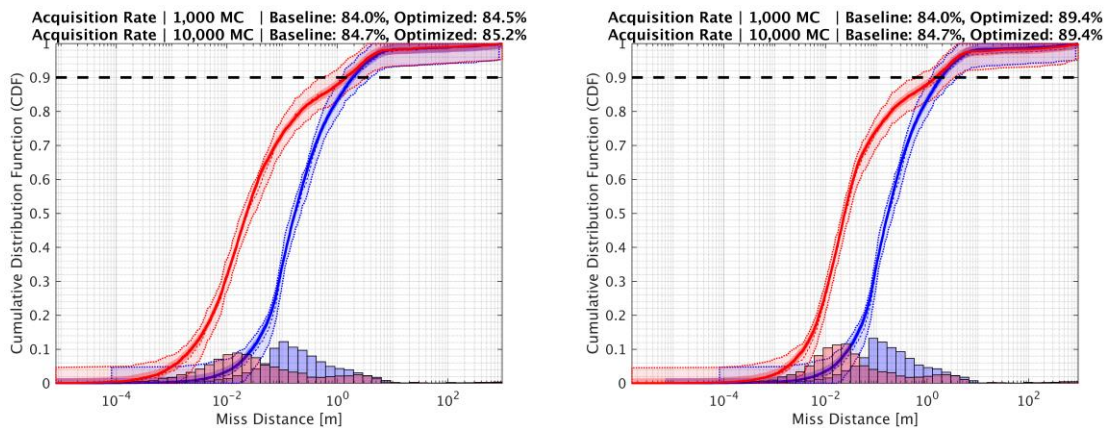
Figure 28. Empirical distribution functions and histograms for the baseline case (*blue*) and optimized guidance and seeker case (*red*) trained with the 20 MC target set (*left*) or the 100 MC target set (*right*).

VI.   Appendix B – 1,000 MC Testing Target Set Trajectories
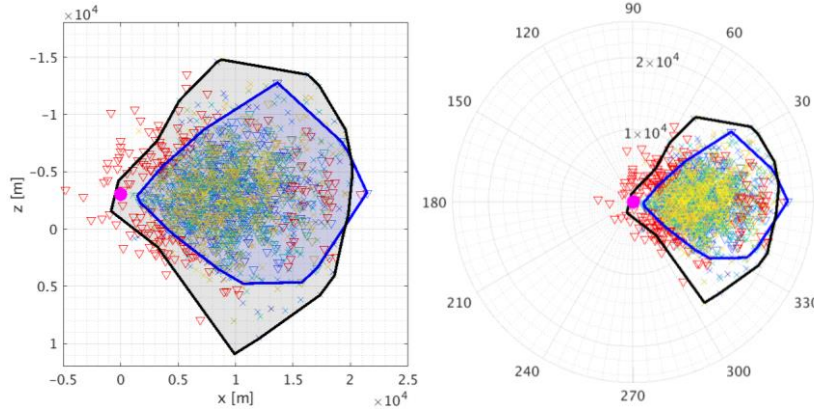
Figure 29. Rectangular (*left*) and polar (*right*) trajectory spaces for the baseline case tested with the 1,000 MC target set.
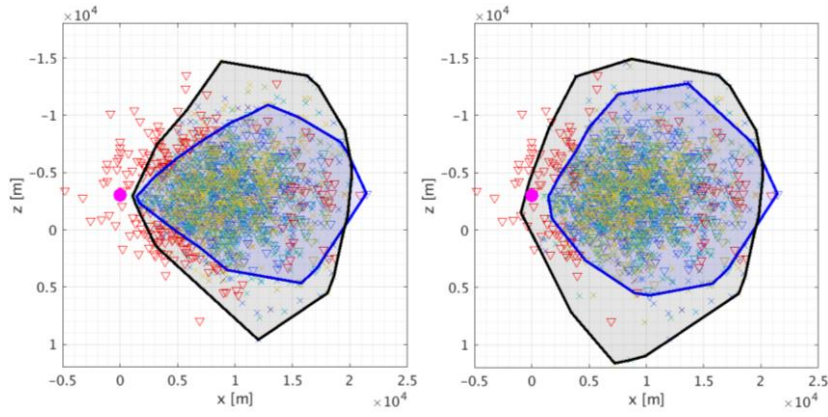

Figure 30. Rectangular trajectory spaces for the optimized seeker case trained with the 20 MC (*left*) and 100 MC (*right*) target sets and tested with the 1,000 MC target set.
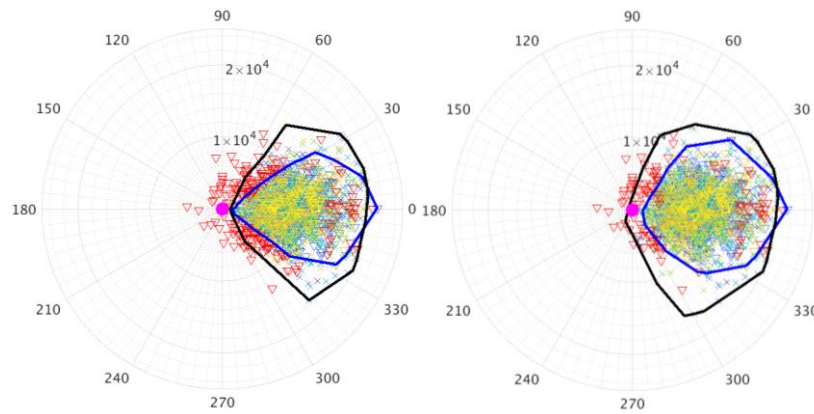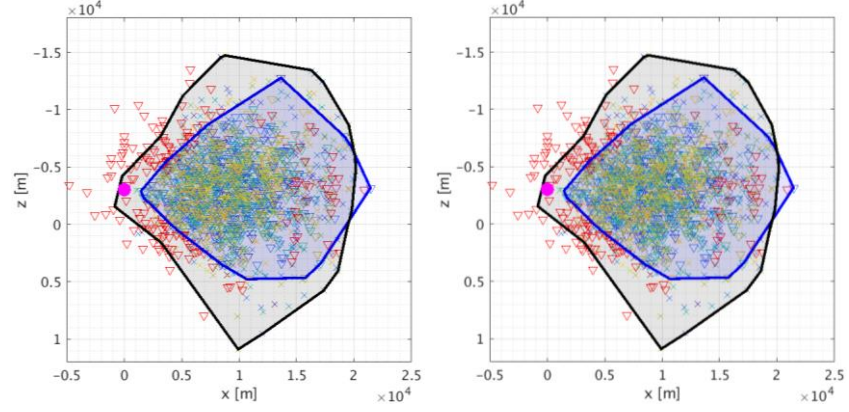

Figure 31. Polar trajectory spaces for the optimized seeker case trained with the 20 MC (*left*) and 100 MC (*right*) target sets and tested with the 1,000 MC target set.

Figure 32. Rectangular trajectory spaces for the optimized guidance case trained with the 20 MC (*left*) and 100 MC (*right*) target sets and tested with the 1,000 MC target set.
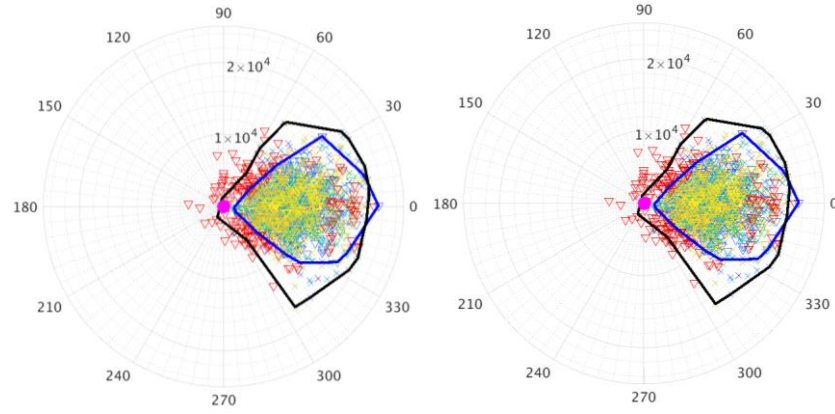

Figure 33. Polar trajectory spaces for the optimized guidance case trained with the 20 MC (*left*) and 100 MC (*right*) target sets and tested with the 1,000 MC target set.
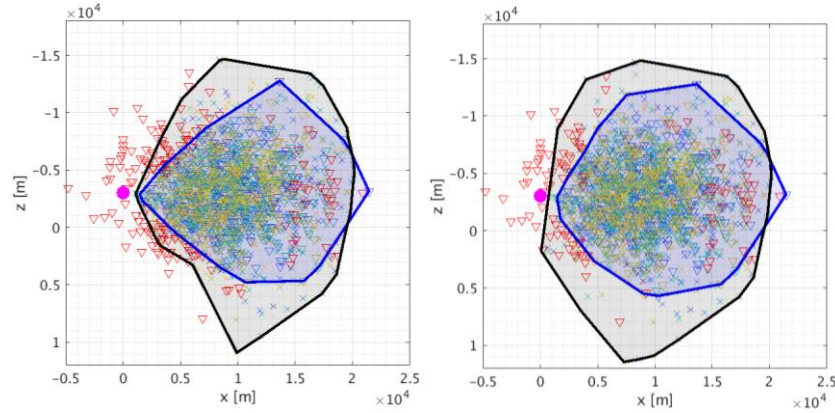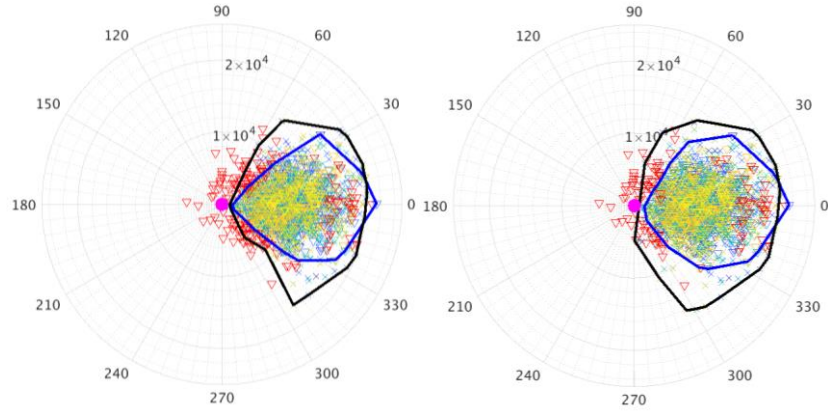

Figure 34. Rectangular trajectory spaces for the optimized guidance and seeker case trained with the 20 MC (*left*) and 100 MC (*right*) target sets and tested with the 1,000 MC target set.

Figure 35. Polar trajectory spaces for the optimized guidance and seeker case trained with the 20 MC (*left*) and 100 MC (*right*) target sets and tested with the 1,000 MC target set.